Astronomy
&
Astrophysics

A systematic study of X-ray substructure of galaxy clusters detected in the ROSAT All-Sky Survey[*]

P. Schuecker[1], H. Böhringer[1], T. H. Reiprich[1], and L. Feretti[2]

[1] Max-Planck-Institut für extraterrestrische Physik, Garching, Germany
[2] Istituto di Radioastronomia CNR, Bologna, Italy

Abstract. Results of a systematic study of substructure in X-ray surface brightness distributions of a combined sample of 470 REFLEX+BCS clusters of galaxies are presented. The fully automated morphology analysis is based on data of the 3rd processing of the ROSAT All-Sky survey (RASS-3). After correction for several systematic effects, 52 ± 7 percent of the REFLEX+BCS clusters are found to be substructured in metric apertures of 1 Mpc radius ($H_0 = 50 \mathrm{~km\,s^{-1}\,Mpc^{-1}}$). Future simulations will show statistically which mass spectrum of major and minor mergers contributes to this number. Another important result is the discovery of a substructure-density relation, analogous to the morphology-density relation for galaxies. Here, clusters with asymmetric or multi-modal X-ray surface brightness distributions are located preferentially in regions with higher cluster number densities. The substructure analysis techniques are used to compare the X-ray morphology of 53 clusters with radio halos and relics, and 22 cooling flow clusters with the REFLEX+BCS reference sample. After careful equalization of the different "sensitivities" of the subsamples to substructure detection it is found that the halo and relic sample tends to show more often multi-modal and elongated X-ray surface brightness distributions compared to the REFLEX+BCS reference sample. The cooling flow clusters show more often circular symmetric and unimodal distributions compared to the REFLEX+BCS and the halo/relic reference samples. Both findings further support the idea that radio halos and relics are triggered by merger events, and that pre-existing cooling flows might be disrupted by recent major mergers.

Key words. galaxies: clusters: general

1. Introduction

Current structure formation scenarios suggest a hierarchical growth of cosmic objects (e.g., Peebles 1980; White 1996) where the merging of subclumps turns out to be a fundamental process. Linear theory predicts that clustering in critical density universes continues to grow up to present-day redshifts, and structure formation begins to decline already at $z \approx \Omega_0^{-1} - 1$ in low density universes, where Ω_0 is the present value of the normalized cosmic matter density. Compared to the Einstein-de Sitter case, clusters in low-Ω_0 universes are thus expected to be more relaxed, less substructured, and less elongated, as shown by the simulations of the Virgo Consortium (see Thomas et al. 1998) and the simulations of Evrard et al. (1993), Crone et al. (1996), Mohr et al. (1995), etc. The frequencies of subclumps (substructures) and elongations are thus useful statistical quantities with a direct relation to

cosmology. See also the analytic work of, e.g., Richstone et al. (1992) and Lacey & Cole (1993). Note, however, that the effects are difficult to measure so that the resulting constraints on structure formation models are presently less stringent compared to, e.g., a direct measurement of the power spectrum of cluster number density fluctuations as presented in, e.g., Schuecker et al. (2001).

Cluster mergers produce moderately supersonic shocks, compressing and heating the intracluster gas, and increasing pressure and entropy. This can be measured as local distortions of the spatial distribution of X-ray temperature and surface brightness (e.g., Schindler & Müller 1993; Roettiger et al. 1997). Moreover, mergers affect cluster X-ray luminosity, magnetic field, and electron/ion non-equipartition (see, e.g., Schindler & Müller 1993; Roettiger et al. 1999, Takizawa 2000, Ricker & Sarazin 2001). Therefore, studies of individual clusters provide a wealth of new and useful information on the physics of the merger process, e.g., from spatially resolved X-ray spectroscopy.

A more detailed study would thus ideally use deep pointed X-ray observations to get high signal-to-noise

temperature and surface brightness maps. Unfortunately, X-ray data from public archives generally allow precise measurements on interesting but not necessarily representative clusters of galaxies. For the majority of the clusters needed for a statistically representative sample, detailed studies are at present and in the near future not achievable. What is needed for cosmological investigations is a systematic and comprehensive study of substructure characteristics for a large set of clusters compiled in an homogeneous way.

Concerning the projected X-ray surface brightness distribution, merger events cause multiple X-ray luminosity peaks, isophote twisting with centroid shifts, elongations, and other irregularities. One of the first systematic studies of such cluster X-ray morphologies was undertaken by Jones & Forman (1999) using the spatial surface brightness distributions of targeted and serendipitous clusters obtained with the *Einstein* imaging proportional counter (IPC). Their visual classifications of the X-ray iso-intensity contours of 208 clusters with $z \leq 0.15$ are useful, but subjective. For refined statistical analyses it should be supplemented by a more homogeneous sample selection and by a more objective, i.e., quantitative method to analyse the cluster morphology. Along this line, Mohr et al. (1995) measured emission-weighted variations of the cluster centroid for substructure detection, but only for a comparatively small sample of 65 bright *Einstein* clusters. The remaining studies not mentioned here are restricted to even smaller cluster samples.

One possibility towards a systematic study of substructure is offered by the large area ROSAT All-Sky Survey (RASS, Trümper 1993; Voges et al. 1999). However, both the energy resolution of 40 percent $FWHM$ at $1\,\mathrm{keV}$ and the limited energy range $0.1 \leq E \leq 2.4\,\mathrm{keV}$ of the ROSAT position-sensitive proportional counter (PSPC) limit temperature measurements of the intracluster gas, especially for $kT \geq 4\,\mathrm{keV}$. This and the fact that the small number of RASS-3 photons counted in the direction of a typical galaxy cluster in our samples do neither allow the determination of useful temperature maps nor the proper quantification of the amount of substructure, e.g., in the form of mass estimates of the individual subclumps for the majority of a fair cluster sample (but see Sect. 8). The present analysis thus gives more weight to a representative study of a large sample of clusters, mainly restricted to substructure detection and significance determination in terms of significance for the degree of substructure for a whole sample or for specific subsamples.

In a series of papers we want to study the morphology of a large set of X-ray clusters in a systematic way. The present paper investigates the morphology of galaxy clusters using the X-ray surface brightness distributions extracted from data obtained in the course of the 3rd processing of the ROSAT All-Sky Survey (RASS-3). Further papers will concentrate on the study of alignment effects of the major cluster axes, and on detailed comparisons with large scale, high resolution numerical simulations. The morphological analyses are mainly restricted to galaxy

clusters of the two largest and almost complete X-ray cluster surveys finished to date: the ROSAT-ESO Flux-Limited X-ray (REFLEX) cluster survey (Böhringer et al. 2001) in the South, and a survey yielding the Brightest Cluster Sample (BCS, Ebeling et al. 1998) in the North.

In the present investigation we also describe more detailed studies of specific cluster types with so-called radio halos and radio relics, and signatures of cooling flows. Reviews concerning the latter cluster type can be found in, e.g., Fabian et al. (1984), and Fabian (1984), but see also Makishima et al. (2001). A few comments concerning the former two cluster types will be given in the following (see also the conference proceedings edited by Böhringer et al. 1999).

Willson (1970) discovered diffuse, cluster-wide, steep spectrum synchrotron emission associated with the intracluster plasma medium. Recent lists of these objects can be found in, e.g., Feretti (1999), Giovannini (1999), Giovannini et al. (1999), Owen et al. (1999), and Giovannini & Feretti (2000). The radio morphology is classified into radio halos and relics depending on whether (almost unpolarized) radio emission is detected throughout the cluster, or (higher polarized) radio emission is detected in the cluster periphery. Radio halos and relics are predominantly found in rich compact clusters with Bautz-Morgan types II-III (Hanisch 1982), have high X-ray luminosities and temperatures, in most cases no cooling flow signature, and large cluster X-ray core radii. It is suggested (see, e.g., Harris et al. 1980; Burns et al. 1995; Feretti & Giovannini 1996, and the review of Sarazin 2001) that radio halos form during the merging of subclusters, accelerating (existing relativistic) particles in shocks formed in the intracluster gas, although additional processes seem to be necessary. Because of the comparatively small sample sizes involved (see Sect. 3) we refer in the following only to the combined radio halo/relic sample, neglecting the interesting differences between the two cluster types.

Section 2 describes the methods used to detect substructure in two-dimensional photon distributions and to assign statistical significances to the results. The REFLEX and BCS samples as well as the radio halo/relic and cooling flow samples are described in Sect. 3. Further tests and illustrations of the morphological classifications are given in Sect. 4. The observed frequency distributions of clusters with substructure are discussed in Sect. 5. The substructure occurrence rates (SORs) show a comparatively strong sensitivity to the number of X-ray photons used for substructure analyses. A simple method to reduce this effect is described.

To proceed further, two methods seem useful. The first possibility is the application of our substructure tests to simulated images where selection effects introduced by observation and data reduction are taken into account. In addition, the comparison with simulations is expected to yield statistical information about the mass spectrum of the merger masses to which our substructure tests are sensitive at various redshifts and X-ray fluxes. This work

is postponed to a later paper. The second possibility is the relative comparison of subsamples extracted from the combined REFLEX+BCS catalogs in a manner that selection effects partially cancel out. The subsequent sections of this paper are devoted to this kind of analysis.

One important result obtained with the latter strategy is the discovery of a substructure-density relation, analogous to the morphology-density relation for galaxies (Sect. 6). Other interesting results are obtained from the relative comparison of substructure significance distributions of halo/relic, cooling flow, and REFLEX+BCS clusters (Sect. 7). Here we create reference subsamples drawn randomly from the REFLEX+BCS sample in such a way that the reference samples have basically the same "sensitivity" for substructure detection as the halo/relic and cooling flow samples. With this method we can compare for the first time the substructuring and elongation behaviour of specific cluster types with a representative large-area cluster sample. A general discussion of the results is given in Sect. 8.

All computations assume Friedmann-Lemaître world models with zero pressure, the Hubble constant $H_0 = 50\,\mathrm{km\,s^{-1}\,Mpc^{-1}}$, the density parameter $\Omega_0 = 1.0$, and the cosmological constant $\Omega_\Lambda = 0$.

2. Statistical tests for substructure

2.1. General considerations

In X-rays, quantitative analyses of substructure are based on detailed fits of elliptical models or wavelets to X-ray isophotes, studies of ellipticities, center-shifts, power ratios, etc. (see, e.g., the review in Buote 2001). However, representative SORs can only be obtained with large cluster samples. The RASS-3 X-ray images of our cluster sample which can be used for this purpose have on average 359 with up to 6829 X-ray photons (in the ROSAT hard energy band, see below) within an aperture of 1 Mpc radius. Therefore, more robust tests for substructure are needed. Unfortunately, the relation between substructure as defined by robust tests and a physical quantification of substructure is less direct and a larger effort is needed for the physical interpretation of the results. The link between SORs and theoretical merger rates can be obtained when the mass scales of the subclumps and the time scales needed for the merged cluster to reach dynamical equilibrium are known. Many observational effects become apparent when statistical samples are analysed (see Sects. 5, 5.1) which complicate the interpretation of SORs. After proper correction, semi-analytic Press Schechter-like theories as presented in, e.g., Lacey & Cole (1993) can in principle be applied to understand the merger rates within a cosmological context.

However, the relation between observed SORs and true substructure becomes secondary when SORs obtained for different subsamples drawn from the same parent distribution are compared. In this case the tests define substructure more operationally as that which they measure,

and they can serve as a mere link between different cluster types as, for example, clusters located in high and low-density regions (Sect. 6) or halo/relic clusters, cooling flow clusters (Sect. 7).

N-body simulations of merging clusters of galaxies favour three tests for the analysis of two-dimensional point distributions (Pinkney et al. 1996). The tests described in Sects. 2.3 to 2.5 are sensitive to different types of substructure and are thus ideally suited for the detection of a large variety of different merger events. We use the three tests and translate them to the case of two-dimensional X-ray images as extracted from the RASS-3 fields. Section 4 compares substructures as defined in the present paper under realistic conditions with the results obtained by other research groups with different methods.

2.2. X-ray survey data

Before the substructure statistics are described the basic properties of the X-ray material used for the analysis are summarized. This will explain some of the constraints already imposed by the observational data. The 1378 RASS-3 fields used for substructure analyses cover the whole sky with an *averaged* spatial resolution as given by the half power radius of 96 arcsec at 1 keV. Substructure on scales larger than approximately $2\,\mathrm{Mpc}\cdot z$ (e.g., 200 kpc at $z = 0.1$) is thus resolved. Within this precision, the point spread function is constant over each RASS field and can be regarded as circular symmetric (G. Boese, private communication). Each field has a size of $6.4 \times 6.4\,\mathrm{deg}^2$ and overlaps at least 0.23 deg with adjacent fields. The main advantage of RASS-3 compared to RASS-2 is that its less stringent constraints on the attitude solutions yield a larger number of accepted X-ray photon events (on average about 5 percent, and is essential only in certain parts of the sky) resulting in a higher signal-to-noise without a significant increase of the measurement errors of the individual photons. The advantages of RASS-2 against RASS-1 are discussed in Voges et al. (1999).

Each of the N_{ph} photons detected in the direction of a cluster of galaxies is characterized by the following quantities. The sky pixel coordinates, (x_i, y_i), given for the ith photon in units of 0.5 arcsec, and the photon energy, E_i, given in the form of a Pulse Height Amplitude (PHA) channel number, are contained in the photon event file of each RASS-3 field. The exposure time, t_i, used to weight each photon, is determined with the exposure map, giving for each RASS-3 field the survey exposure times, corrected for vignetting and the effect of the shadowing of the support structure of the PSPC window with a spatial binning of 45 arcsec. We do not differentiate between source and background photons because no distinction can be made on the photon-by-photon basis.

Only X-ray photons selected from the ROSAT hard energy band (PHA channels 52 to 201 corresponding to about 0.5–2.0 keV) are used for all reductions. This reduces the soft X-ray background by a factor of 4, but

still keeps 60 to 100 percent (depending on the interstellar column density) of the cluster emission. Moreover, the majority of soft RASS-3 sources superposed onto the cluster images are suppressed, so that the signal-to-noise for cluster detection is highest.

Since comparatively large samples of clusters have to be analyzed the computer-intensive substructure tests had to be simplified (see below). The tests are performed within one aperture with the metric radius of 1.0 Mpc centered on the X-ray intensity-weighted center of the cluster. The iterative determination of the cluster center terminates when a formal accuracy of 2 arcsec is reached (for more details see Böhringer et al. 2000, 2001).

2.3. The β test

The β statistic compares the surface number density, μ_i, measured in the ith radial segment with the density, μ_{oi}, measured in the diametrically opposite segment. The number densities are obtained by weighting each photon with the corresponding exposure time. The final β value is the average of the ratios obtained over all independent N_s radial segments (typically 8):

$$\beta = \frac{1}{N_s} \sum_{i=1}^{N_s} \log_{10} \left(\frac{\mu_i}{\mu_{oi}} \right). \tag{1}$$

This test is a simplified version of a method developed by West et al. (1988).

As noted in Pinkney et al. (1996) the β value (in its original definition) is sensitive to deviations from mirror symmetry, independent of the actual elongation of the target. The statistic becomes rather ineffective as the mass ratio of the sub-components approaches 1:1. We expect similar properties of the presently implemented simplified version. Note that the application of radial segments instead of individual photon coordinates is used to make the test more robust and to save computing time although this might desensitize the test. The actual sensitivity of the β parameter is tested with RASS-3 images in Sect. 4.

2.4. The Lee test

In the Lee statistic the photons are projected onto lines with given inclination angles, ϕ (12 directions in the present implementation). In general, for all ϕ and for all partitions of the set of photons, the "within-class" scatter, $\sigma_L + \sigma_R$, and the "between-class" scatter, σ_T, are determined and their ratios, $\sigma_T/(\sigma_L + \sigma_R)$, maximized. We use the test based on the technique of maximum likelihood in the form

$$L = \frac{L_{\max}}{L_{\min}} = \frac{\max_\phi \{L(\phi)\}}{\min_\phi \{L(\phi)\}}, \tag{2}$$

where

$$L(\phi) = \max_{\{\text{partitions}\}} \left(\frac{\sigma_T}{\sigma_L + \sigma_R} - 1 \right) \tag{3}$$

gives the maximum likelihood obtained for the $(N_{ph} - 1)$ partitions. The partitions are obtained by dividing the total set of photon coordinates (T) projected onto a line with a given ϕ into a right (R) and a left (L) subgroup with the corresponding scatters

$$\sigma_\alpha = \sum_{j=1}^{K_\alpha} w_j (x_j - \bar{x}_\alpha)^2, \qquad \bar{x}_\alpha = \frac{\sum_{j=1}^{K_\alpha} w_j x_j}{\sum_{j=1}^{K_\alpha} w_j}, \tag{4}$$

where $\alpha = T, R, L$, the weighting factor for the ith photon is $w_j = 1/t_j$, and K_α is the actual number of projected points in the T, R, L samples. More details can be found in Fitchett et al. (1988). Fitchett & Webster (1987) successfully applied the method for substructure detection in the core of the Coma galaxy cluster.

The likelihood value, L, is most sensitive if two substructure components are present, especially when they are very compact. It is not sensitive to any elongations and loses sensitivity if more than two subclumps are visible. Compared to the other two tests the LEE statistic is thus the most conservative.

2.5. The Fourier elongation test

Deviations from circular symmetry might indicate merger events (e.g., Roettiger et al. 1997, see also Buote 2001), although relaxed clusters can show significant ellipticities too as illustrated in Sect. 4. However, recent simulations of Thomas et al. (1998) and others (see Sect. 1) clearly show a dependency of the frequency distribution of cluster major axial ratios on cosmology, where the rounder X-ray isophotes in the low-Ω_0 models might result primarily from the scarcity of recent mergers (Evrard et al. 1993). We thus regard elongation as a useful cosmological quantity although its relation to substructure appears to be more complicated.

Following Rhee et al. (1991) the azimuthal number counts are approximated to first order by a constant density, modulated by a double sine. Under this assumption the normalized amplitude of this modulation,

$$\text{FEL} = \sqrt{\frac{2(S^2 + C^2)}{N_0}}, \tag{5}$$

gives a measure of the elongation strength. The parameters S and C are defined by Eq. (7) in Pinkney et al. (1996). The position angle is then $\text{PA} = 0.5 \arctan(S/C)$. We translate (5) to the unbinned case, where each photon is weighted by its exposure time,

$$S = \sum_{i=1}^{N_{ph}} \frac{2x_i y_i}{t_i (x_i^2 + y_i^2)}, \qquad C = \sum_{i=1}^{N_{ph}} \frac{x_i^2 - y_i^2}{t_i (x_i^2 + y_i^2)}, \tag{6}$$

with $N_0 = \sum_i 1/t_i$. The N-body simulations show that FEL is the most sensitive of the three tests used to check for substructure if elongation is to be considered as substructure.

2.6. Statistical significances

In the following the method is described which is used to compute the probabilities (statistical significances S) that the actual values of the substructure parameters described in Sects. 2.3 to 2.5 could be obtained just by chance from an X-ray image satisfying the null hypothesis of a circular symmetric, mirror-symmetric, and unimodal surface brightness distribution. The statistical significance, S, thus corresponds to the confidence probability, $(1 - S)$, that the null hypothesis can be rejected.

The significance values, S_β, S_{FEL}, S_{LEE}, are computed by comparing the β, FEL, and L values obtained for the programme cluster with the corresponding values obtained with a large set of unstructured photon distributions (replicants) derived from the same cluster. For the position-independent, circular symmetric average point spread function of RASS-3 (see Sect. 2.2), these smooth and symmetric distributions can be obtained by azimuthal randomization (West et al. 1988), keeping the radial distances of the original X-ray photons, but assigning random angular coordinates without the need to choose a specific (model) cluster profile.

The significances are computed as follows. In the first step β, FEL, and L are computed for the programme cluster. In the next step the photon distribution is azimuthally randomized, and for each randomized cluster, β', FEL$'$, and L' are computed again. The primes denote values of the statistics obtained with the randomized distribution. As seen above the statistics are normalized in such a way that larger values correspond to larger substructures. Therefore, the number of times the randomized distribution gives a value larger than that obtained for the programme cluster provides an estimate of the probability, S, that the actual substructure value can be obtained just by chance from a cluster fulfilling the null hypothesis. Notice that small values of S correspond to clusters with substructure and elongation.

To be more specific, the substructure analyses are performed and statistical significances are computed for one aperture with the metric radius of 1.0 Mpc. This metric scale is transformed into an angular scale with the cluster redshift using the angular diameter distance. The choice of this radius guarantees that in the majority of cases the outer significance radii of the X-ray images, defined below, include the aperture used to evaluate substructure. For larger apertures, contributions from neighbouring clusters and chance superposition of background sources become more important. The significance radius is defined in Böhringer et al. (2000, 2001) as the point where the increase in the 1σ flux error is larger than the increase of the cumulative source count rate after background subtraction. For the β and FEL statistic, 2000 replicants are used for each cluster, for the most time-consuming LEE statistic 400 replicants.

3. Cluster samples

The REFLEX sample (Böhringer et al. 2001) includes 452 clusters (449 with redshifts), detected in the RASS-2 database (Voges et al. 1999) south of the Declination $+2.5\,$deg and down to the nominal X-ray flux limit of $3.0 \times 10^{-12}\,\text{erg s}^{-1}\,\text{cm}^{-2}$ in the ROSAT energy band $(0.1-2.4\,\text{keV})$. REFLEX covers $4.24\,$sr excluding the area $\pm 20\,$deg around the galactic plane and $0.0987\,$sr around the Magellanic Clouds and is basically restricted to redshifts $z \leq 0.3$ (a few clusters reach $z = 0.45$). The Growth Curve Analysis method of Böhringer et al. (2000, 2001) is used to compute source positions, fluxes, angular extents, etc. (source characterization). The catalog gives unabsorbed X-ray fluxes with statistical errors between 10 and 20 percent. Several tests indicate a high overall completeness of the sample (at least 90 percent) with an upper limit of 10 percent of the clusters with fluxes significantly contaminated by active galactic nuclei (AGN).

The BCS sample (Ebeling et al. 1998) includes 201 clusters (statistical sample), detected north of the Declination $\delta = 0\,$deg, excluding the area $\pm 20\,$deg around the galactic plane using the RASS-1 data. The formal flux limit of the resulting sample is $4.4 \times 10^{-12}\,\text{erg s}^{-1}\,\text{cm}^{-2}$ $(0.1-2.4\,\text{keV})$. The Voronoi Tesselation and Percolation method (first version of the method described in Ebeling & Wiedenmann 1993) is used to obtain unabsorbed X-ray fluxes. The authors estimated a sample completeness of 90 percent for the 201 BCS clusters with $z \leq 0.3$. Some artificial fluctuations in cluster number density might occur because the clusters are not sampled homogeneously over the total survey area given in Ebeling et al. (1998). For the present investigation the effects can be neglected because only large-amplitude fluctuations (>10 precent) are discussed.

There are basically two motivations for using a combined sample of REFLEX and BCS clusters for our substructure analysis. (1) It is expected that the results of substructure analyses are improved when more X-ray photons are available (see Sect. 5). Combining the REFLEX and BCS catalogues to an all-sky sample and cutting it at the flux limit of the brighter BCS sample yields the largest number of X-ray images with high numbers of X-ray photons. (2) Due to the fact that at low redshifts the northern BCS sample might be dominated by the local supercluster and its extension, and the southern REFLEX sample by the southern void (e.g., Schuecker et al. 2001), the merged REFLEX and BCS catalogue is expected to provide a more representative sample.

To ensure an homogeneous handling of the data we exclude the Virgo cluster because of its large angular extent. Furthermore, A689, Z3179, and RXC J1212.3-1817 are excluded because of their low ROSAT exposure times (too few photons), A1678 and RXC J0532.9-3701 which are located too close to the RASS-3 field edge, and three further REFLEX clusters where redshift information is not yet available. The combined sample referred to as REFLEX+BCS contains 470 clusters (excluding the
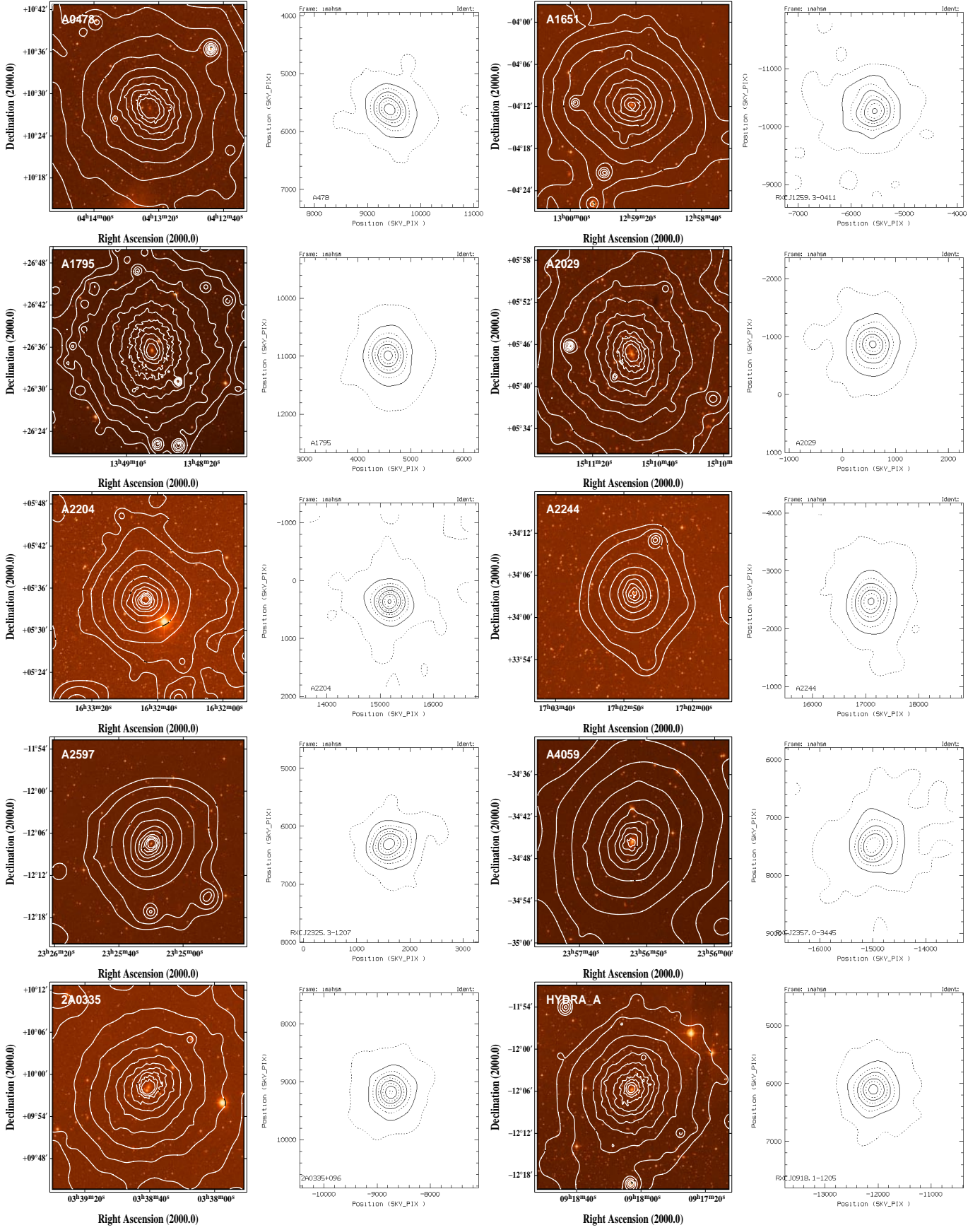
Fig. 1. Comparison of iso-surface brightness contours of deep ROSAT PSPC pointings (first and third columns) and corresponding RASS-3 images (second and fourth columns) of regular clusters. The pointings are superposed on Digital Sky Survey optical images. Source characterizations are given in Table 1 (clusters 1–10).
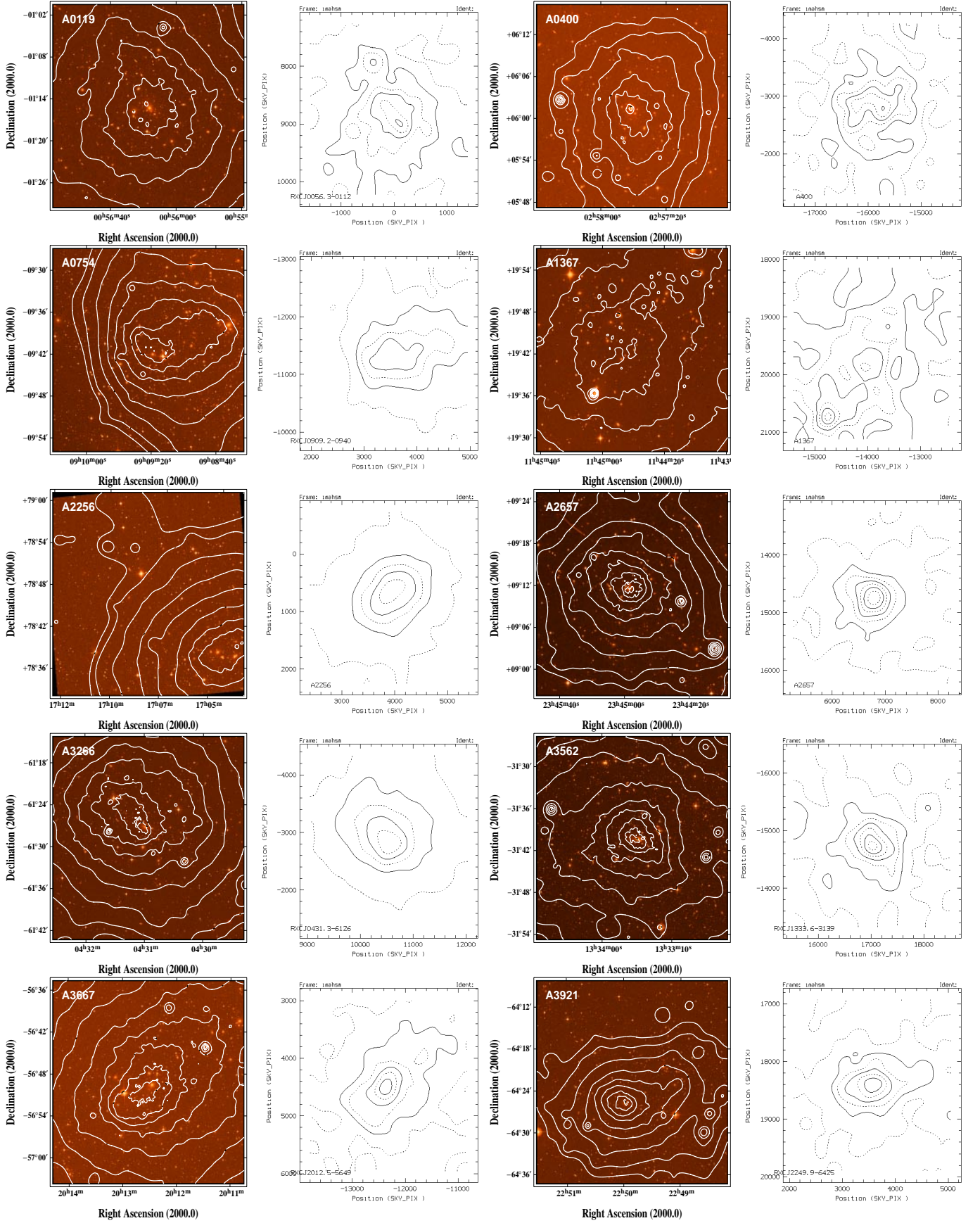
Fig. 2. Comparison of iso-surface brightness contours of deep ROSAT PSPC pointings (first and third columns) and corresponding RASS-3 images (second and fourth columns) of substructured clusters. The pointings are superposed on Digital Sky Survey optical images. Source characterizations are given in Table 2 (clusters 11–20).

BCS clusters in common with REFLEX) with a formal flux limit of $4.4 \times 10^{-12} \, \mathrm{erg \, s^{-1} \, cm^{-2}}$. Although BCS and REFLEX fluxes are computed with different algorithms on different RASS versions no problems are expected because each version has its own calibrations.

A sample of 53 halo and relic clusters (including six uncertain cases) compiled by Feretti et al. (in preparation) is used to study the statistical properties of their X-ray morphology. In the following we use the combined halo/relic sample as mentioned in Sect. 1. Deep pointings obtained mainly with ROSAT suggest that eventually all of these clusters show distorted X-ray surface brightness distributions. Presently no information about the completeness of this sample is available. In the present investigation RASS-3 data are used for their analysis so that the substructure tests can be directly compared to the statistically representative REFLEX+BCS reference sample.

A sample of 22 clusters with large cooling flow signatures is selected from the list presented in Peres et al. (1998). Their total sample of 55 clusters with fluxes above $1.7 \times 10^{-11} \, \mathrm{erg \, s^{-1} \, cm^{-2}}$ in the $2-10 \, \mathrm{keV}$ energy band is selected from observations with the *Einstein* and EXOSAT observatories, and the HEAO-1 and Ariel V satellites by Edge et al. (1990) and is found to be "satisfactorily complete". The selected cooling flow clusters have mass deposition rates larger than $100 \, M_{\odot} \, \mathrm{yr}^{-1}$ as determined by a surface brightness deprojection technique using ROSAT PSPC and HRI pointed observations. Notice that for the present investigation only the cooling flow signature of a steep increase of the central X-ray surface brightness matters, and that a possibly new interpretation of cooling flows due to the non-detection of cooling gas with temperatures below about $3 \, \mathrm{keV}$ in XMM spectra (Peterson et al. 2001) is secondary. The majority of the clusters in the sample have $z \leq 0.1$.

4. Verification of the method

The methods used for substructure detection were analyzed and tested in detail with numerical N-body simulations (Pinkney et al. 1996). Here we want to illustrate the types of substructures to which the three substructure tests are sensitive under realistic conditions comparing deep ROSAT pointed observations and the corresponding RASS-3 images of clusters with known morphology and substructure behaviour (see Sect. 4.1). In addition, we want to study the relation between the substructure tests and the Jones & Forman classification scheme to allow a reference to a similar systematic survey project (see Sect. 4.2). It will be seen that the three substructure statistics provide a quantitative morphological classification of RASS-3 images which has a close relation to substructure as defined and quantified with other methods and data.

4.1. Comparison with deep ROSAT PSPC pointings

Figures 1 and 2 show a collection of 10 regular and 10 substructured "prototype" clusters as obtained with deep ROSAT PSPC pointings (1st and 3rd Cols.) and the corresponding RASS-3 images (2nd and 4th Cols.) used for our substructure analyses. Literature information and the significances obtained with our substructure tests using RASS-3 data within a metric aperture of 1.0 Mpc are summarized in Tables 1 and 2. From the literature we summarize the classifications obtained with the power ratio technique from ROSAT PSPC pointed observation by Buote & Tsai (1996), cooling flow mass deposition rates and cooling times as derived by Peres et al. (1998) using ROSAT PSPC and HRI data, centroid variances deduced by Mohr et al. (1995), and visual classifications of Jones & Forman (1999), both obtained with *Einstein* IPC data, ellipticities and center-of-mass shifts as deduced from Abell+APM galaxy and ROSAT X-ray data by Kolokotronis et al. (2000), and results obtained with the adaptive-kernel technique by Kriessler & Beers (1997) using optical galaxies in Dressler's clusters. We also add the presence of cold fronts as given in Markevitch et al. (2000) and Vikhlinin et al. (2001).

The clusters shown in Fig. 1 are nearby $z < 0.1$ clusters, all with strong cooling flow signatures and classified as single, regular, smooth, and/or no centroid shift by the authors given in Tables 1 and 2. The S_{LEE} significances as obtained from the RASS-3 images range between 0.13 and 0.96, the S_{β} values between 0.06 and 0.76, and the S_{FEL} values between 0.0 and 0.81. Assuming a 99 percent confidence level none of the LEE and β tests indicate significant substructure for these clusters. According to our substructure statistics, clusters like A478 and A4059 show a significant ellipticity, including A1795, A2244, A2597 on the 97 percent confidence level (in total 5 out of the 10 clusters). If we assume that the central 1.0 Mpc of these clusters, where the tests are performed, are dynamically relaxed and unstructured then ellipticity and thus FEL would turn out to be a less useful indicator for substructure whereas β and LEE would do.

The non-regular clusters shown in Fig. 2 have negligible cooling flows; some have cold fronts. The clusters are classified as substructured by different authors using various methods and data (X-ray, optical). For A754, A1367, and A3266 the β, LEE, and FEL tests all give zero probability for the null hypothesis, thus strongly suggesting substructured RASS-3 surface brightness distributions. For A119, A2256, and A3667 either the β and/or the LEE test suggest the presence of substructure. On the 98 percent confidence level this is also true for A400, A2657, A3562, and A3921. Therefore, basically all 10 prototype clusters shown here are recovered as substructured on the 98 percent confidence level with the β and/or LEE test on RASS-3.

We found a good correspondence between the position angles, PA, as seen in the deep pointings and as obtained from the RASS-3 images (given in Tables 1 and 2). The position angles are obtained with both the FEL method and with surface brightness-weighted moments. In basically all cases with elongation significances $S_{\mathrm{FEL}} \leq 0.01$, position angles obtained with the FEL method and those

Table 1. Characterization of the regular galaxy clusters shown in Fig. 1. The mass deposition rates are in units of solar mass per year as obtained from ROSAT PSPC/HRI pointings, S_{LEE}, S_β, S_{FEL} are the statistical significances obtained with the RASS-3 images within circles of radius R in arcmin corresponding to a metric radius of $1.0\,\text{Mpc}$, position angles, PA in degrees as obtained with FEL and surface brightness-weighted moments.

Cluster	Characterization	Reference
1 A478	smooth	Buote & Tsai (1996)
	no centroid shift	Mohr et al. (1995)
	$\dot{M} = 520-616$	Peres et al. (1998)
	$R = 8'$: $S_{\text{LEE}} = 0.28$, $S_\beta = 0.76$, $S_{\text{FEL}} = 0.00$, PA $= 58/57$	
2 A1651	mostly smooth+ regular	Buote & Tsai (1996)
	$\dot{M} = 138$	Peres et al. (1998)
	$R = 8'$: $S_{\text{LEE}} = 0.56$, $S_\beta = 0.47$, $S_{\text{FEL}} = 0.53$, PA $= 100/105$	
3 A1795	smooth + regular	Buote & Tsai (1996)
	$\dot{M} = 381/488$	Peres et al. (1998)
	$R = 10'$: $S_{\text{LEE}} = 0.15$, $S_\beta = 0.64$, $S_{\text{FEL}} = 0.03$, PA $= 20/12$	
4 A2029	regular + smooth	Buote & Tsai (1996)
	$\dot{M} = 554/556$	Peres et al. (1998)
	$R = 9'$: $S_{\text{LEE}} = 0.87$, $S_\beta = 0.07$, $S_{\text{FEL}} = 0.81$, PA $= 169/176$	
5 A2204	smooth	Buote & Tsai (1996)
	$\dot{M} = 843/852$	Peres et al. (1998)
	$R = 5'$: $S_{\text{LEE}} = 0.59$, $S_\beta = 0.45$, $S_{\text{FEL}} = 0.17$, PA $= 77/92$	
6 A2244	regular	Buote & Tsai (1996)
	$\dot{M} = 244$	Peres et al. (1998)
	$R = 7'$: $S_{\text{LEE}} = 0.13$, $S_\beta = 0.10$, $S_{\text{FEL}} = 0.02$, PA $= 6/174$	
7 A2597	very symm. + smooth	Buote & Tsai (1996)
	$\dot{M} = 276/271$	Peres et al. (1998)
	$R = 8'$: $S_{\text{LEE}} = 0.16$, $S_\beta = 0.49$, $S_{\text{FEL}} = 0.02$, PA $= 93/112$	
8 A4059	smooth, single-comp.	Buote & Tsai (1996)
	$\dot{M} = 130$	Peres et al. (1998)
	$R = 13'$: $S_{\text{LEE}} = 0.96$, $S_\beta = 0.30$, $S_{\text{FEL}} = 0.01$, PA $= 127/130$	
9 2A0335	$\dot{M} = 242/325$	Peres et al. (1998)
	$R = 18'$: $S_{\text{LEE}} = 0.65$, $S_\beta = 0.06$, $S_{\text{FEL}} = 0.52$, PA $= 132/146$	
10 Hydra A	regular	Buote & Tsai (1996)
	$\dot{M} = 298/264$	Peres et al. (1998)
	$R = 12'$: $S_{\text{LEE}} = 0.35$, $S_\beta = 0.37$, $S_{\text{FEL}} = 0.66$, PA $= 140/126$	

determined with surface brightness-weighted moments are found to be very similar within a few degrees.

Moreover, 7 of the 10 clusters (A754, A1367, A2256, A2657, A3266, A3667, A3921) have a significant ellipticity. This suggests a correlation between substructure and the detection of ellipticity. However, as the analysis of the cooling flow clusters already showed, ellipticity as a sole criterion for substructure might not be sufficient for substructure detection. Nevertheless a final decision whether ellipticity is regarded as substructure is not necessary for the present investigation.

In addition to the 20 prototype clusters discussed above, Table 3 summarizes the significances obtained for 43 clusters included in the HIghest X-ray FLUx Galaxy Cluster Sample (*HIFLUGCS*, see the sample description in Reiprich & Böhringer 2001) which have ROSAT PSPC pointed observations and reliable literature information of the kind given in Tables 1 and 2 about the presence or absence of substructure (see the references given at the beginning of this section). The mean significances (Mean1) and their formal 1σ deviations (Std1) given in Table 3

show a clear trend towards smaller significances for the clusters expected to be substructured. This trend is even stronger when mean and standard deviation are computed for the minimum values

$$S = \min\left\{S_{\text{LEE}}, S_\beta\right\}, \tag{7}$$

as given by the Mean2 and Std2 values in Table 3. The last statistic (7) assumes that either a low S_{LEE} or S_β value already indicates substructure which seems to be reasonable in the light of the discussion of individual clusters given above.

4.2. Comparison with Jones & Forman classifications

Jones & Forman (1999) used the iso-intensity contour plots of the *Einstein* IPC X-ray emission of 208 targeted and serendipitously found clusters with $z \leq 0.15$ to classify their morphology into the following categories. *Single*: no substructure or departures from symmetry. *Double*: two subclusters of comparable size and luminosity. *Primary with small secondary*: main subcluster at least two times

Table 2. Characterization of the substructured galaxy clusters shown in Fig. 2. The mass deposition rates are in units of solar mass per year as obtained from ROSAT PSPC/HRI pointings, S_{LEE}, S_β, S_{FEL} are the statistical significances obtained with the RASS-3 images within circles of radius R in arcmin corresponding to a metric radius of 1.0 Mpc, position angles PA in degrees as obtained with FEL and surface brightness-weighted moments.

Cluster	Characterization	Reference	
11	A119	emission tail	Buote & Tsai (1996)
		opt. substructured	Kriessler & Beers (1997)
		centroid shift	Mohr et al. (1995)
		$\dot{M} = 0$	Peres et al. (1998)
		$R = 14'$: $S_{\mathrm{LEE}} = 0.84$, $S_\beta = 0.00$, $S_{\mathrm{FEL}} = 0.13$, PA $= 17/27$	
12	A400	irregular	Buote & Tsai (1996)
		centroid shift	Mohr et al. (1995)
		$R = 25'$: $S_{\mathrm{LEE}} = 0.02$, $S_\beta = 0.34$, $S_{\mathrm{FEL}} = 0.11$, PA $= 176/155$	
13	A754	clearly off center	Buote & Tsai (1996)
		opt. substructured	Kriessler & Beers (1997)
		centroid shift	Mohr et al. (1995)
		$\dot{M} = 0/2$	Peres et al. (1998)
		Radio halo + relic	Cohen et al. (2001)
		Cold Front	Markevitch et al. (2000)
		$R = 12'$: $S_{\mathrm{LEE}} = 0.00$, $S_\beta = 0.00$, $S_{\mathrm{FEL}} = 0.00$, PA $= 101/101$	
14	A1367	centroid shift	Mohr et al. (1995)
		$\dot{M} = 8/0$	Peres et al. (1998)
		$R = 28'$: $S_{\mathrm{LEE}} = 0.00$, $S_\beta = 0.00$, $S_{\mathrm{FEL}} = 0.00$, PA $= 146/145$	
15	A2256	unrelaxed	Buote & Tsai (1996)
		elliptical	Jones & Forman (1999)
		substructured core	Mohr et al. (1995)
		$\dot{M} = 0/0$	Peres et al. (1998)
		Radio halo + relic	Feretti (1999)
		$R = 11'$: $S_{\mathrm{LEE}} = 0.00$, $S_\beta = 0.03$, $S_{\mathrm{FEL}} = 0.00$, PA $= 128/128$	
16	A2657	bi-modal	Buote & Tsai (1996)
		opt. substructured	Kriessler & Beers (1997)
		$R = 15'$: $S_{\mathrm{LEE}} = 0.02$, $S_\beta = 0.23$, $S_{\mathrm{FEL}} = 0.00$, PA $= 77/85$	
17	A3266	substructured core	Mohr et al. (1995)
		strong substructure	Kolokotronis et al. (2000)
		$\dot{M} = 0/3$	Peres et al. (1998)
		$R = 11'$: $S_{\mathrm{LEE}} = 0.00$, $S_\beta = 0.00$, $S_{\mathrm{FEL}} = 0.00$, PA $= 65/63$	
18	A3562	distorted/not ellip.	Buote & Tsai (1996)
		$\dot{M} = 37$	Peres et al. (1998)
		$R = 12'$: $S_{\mathrm{LEE}} = 0.68$, $S_\beta = 0.02$, $S_{\mathrm{FEL}} = 0.60$, PA $= 94/61$	
19	A3667	elongated + distort.	Buote & Tsai (1996)
		apparent bi-modal	Kolokotronis et al. (2000)
		$\dot{M} = 0$	Peres et al. (1998)
		Cold Front	Vikhlinin et al. (2001)
		2 radio relics	Feretti (1999)
		$R = 11'$: $S_{\mathrm{LEE}} = 0.00$, $S_\beta = 0.80$, $S_{\mathrm{FEL}} = 0.00$, PA $= 133/113$	
20	A3921	irregular/merger	Buote & Tsai (1996)
		apparent bi-modal	Kolokotronis et al. (2000)
		$R = 7'$: $S_{\mathrm{LEE}} = 0.02$, $S_\beta = 0.88$, $S_{\mathrm{FEL}} = 0.00$, PA $= 99/102$	

brighter than secondary. *Complex*: more than two subclusters. *Elliptical*: elliptical X-ray surface brightness contours. *Off center*: peak emission not in center defined by lower surface brightness emission. *Galaxy*: emission dominated by a galaxy. The *Einstein* and RASS-3 X-ray images have similar angular resolutions (about 1 arcmin). Moreover, the *Einstein* classifications are restricted to clusters with redshifts $z \leq 0.15$. Therefore, one should expect some correlation between the Jones & Forman and our classifications.

For the comparison of the two classification schemes we follow first Jones & Forman and decide that only the *Single* and *Galaxy* types are regarded as regular and almost relaxed structures. The remaining classes (*Double*, *Primary with small secondary*, *Complex*, *Elliptical*, *Off center*) are regarded as clusters with significant substructure. At this stage we do not doubt the classification of Jones & Forman because we only want to illustrate the relation between two classification schemes.

Table 3. Selected *HIFLUGCS* clusters and their statistical significances for the LEE, β, and FEL statistics for regular (Reg), possibly substructured (Poss), and substructured (Sub) clusters. The significances are obtained from RASS-3 images, the classification of the clusters is taken from the literature. Mean significances (Mean1) and their formal standard deviation (Std1) as well as the mean significances (Mean2) and their standard deviation (Std2) obtained for the minimum values of $(S_{\rm LEE}, S_\beta)$ are given in the last rows (Eq. (7)). Notice that A85 has a substructure just outside the 1 Mpc aperature and is thus regarded as possibly substructured.

	Reg				Poss				Sub		
Name	$S_{\rm LEE}$	S_β	$S_{\rm FEL}$	Name	$S_{\rm LEE}$	S_β	$S_{\rm FEL}$	Name	$S_{\rm LEE}$	S_β	$S_{\rm FEL}$
A478	0.28	0.76	0.00	A85	0.48	0.21	0.00	A119	0.84	0.00	0.13
A1651	0.56	0.47	0.53	A133	0.59	0.11	0.13	A400	0.02	0.34	0.11
A1795	0.15	0.64	0.03	A401	0.07	0.22	0.03	A496	0.01	0.14	0.00
A2029	0.87	0.07	0.81	A2063	0.70	0.01	0.77	A754	0.00	0.00	0.00
A2052	0.80	0.02	0.06	A3158	0.01	0.13	0.00	A1367	0.02	0.00	0.00
A2204	0.59	0.45	0.17	A3558	0.07	0.06	0.00	A2142	0.04	0.00	0.05
A2244	0.13	0.10	0.02					A2147	0.00	0.00	0.00
A2589	0.01	0.39	0.00					A2255	0.00	0.00	0.00
A2597	0.16	0.49	0.02					A2256	0.00	0.03	0.00
A3112	0.39	0.90	0.02					A2634	0.02	0.01	0.02
A3581	0.13	0.96	0.13					A2657	0.02	0.23	0.00
A4038	0.00	0.95	0.00					A3266	0.00	0.00	0.00
A4059	0.96	0.30	0.01					A3376	0.00	0.00	0.00
MKW3s	0.24	0.44	0.21					A3391	0.00	0.46	0.00
Hydra-A	0.35	0.37	0.66					A3395	0.00	0.00	0.00
S1101	0.73	0.11	0.62					A3562	0.68	0.02	0.60
2A0335	0.65	0.06	0.52					A3571	0.00	0.92	0.00
								A3667	0.00	0.80	0.00
								A3921	0.02	0.88	0.00
								RX J2344	0.04	0.02	0.06
Mean1	0.412	0.440	0.224		0.320	0.123	0.155		0.086	0.193	0.049
Std1	0.075	0.077	0.068		0.124	0.034	0.125		0.052	0.071	0.030
Mean2	0.194				0.078				0.006		
Std2	0.038				0.031				0.002		

In total 116 classified *Einstein* clusters are found in common with the REFLEX and BCS sample and are regarded as a representative test sample. Let us first show the relation of the three statistical significances with the classifications of Jones & Forman without introducing an ad hoc threshold for the confidence limit. Figure 3 compares the average significances obtained with each of the three statistics for the clusters classified by Jones & Forman as regular (upper continuous lines including their formal 1σ Poisson errors) and substructured (lower dashed curves). The average significances are computed for subsamples as a function of the minimum number of X-ray photons, $N_{\rm min}$, in the RASS-3 images.

For all $N_{\rm min}$ values a clear trend is seen that clusters classified by Jones & Forman as regular have on average larger significances compared to the clusters classified by Jones & Forman as substructured. The largest differences between the mean S values of regular and substructured clusters are seen for the elongation statistic. This indicates that elongation or ellipticity is comparatively easy to classify both by eye and machine, especially for large $N_{\rm min}$. Similar results supporting the robustness of this criterion are given in Sect. 5.1.

In the next step we want to illustrate the conditions under which our substructure tests give a zero-order quantitative implementation of the Jones & Forman morphological classification scheme although the X-ray data used for the two sets of classifications are different. This also includes the introduction of a fixed confidence level for substructure classification. Consistent with the results obtained in Sect. 4.1 we now assume that clusters which are classified by Jones & Forman as elliptical are in fact unstructured. In order to get higher signal-to-noise surface brightness distributions and thus more reliable substructure detections, we restrict the test sample to those clusters which have at least 200 X-ray photons on the corresponding RASS-3 images. This leaves 73 clusters for the final comparison.

From this test sample, 59 are classified as regular and 14 as substructured by Jones & Forman. We compare
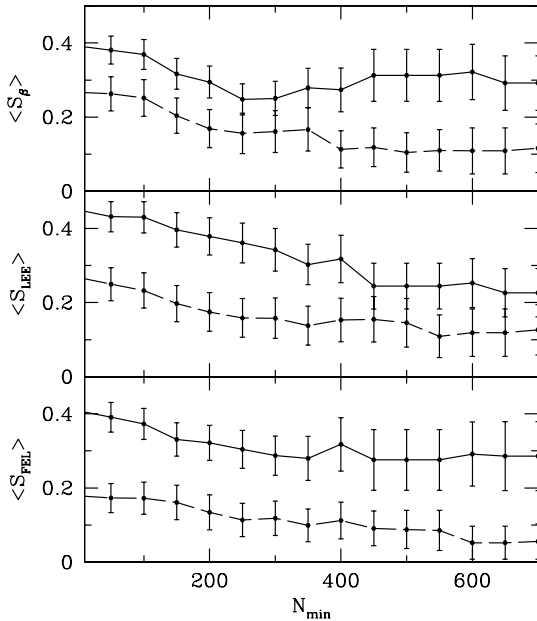
Fig. 3. Average significances and their standard deviation as a function of the number of RASS-3 photons of the 116 *Einstein* clusters in common with the BCS and REFLEX cluster samples. The upper curves in each of the three panels is obtained for the *Einstein* clusters classified as single by Jones & Forman (1999), the lower curves for the *Einstein* clusters classified as double, primary with small secondary, complex, elliptical, or offset center.
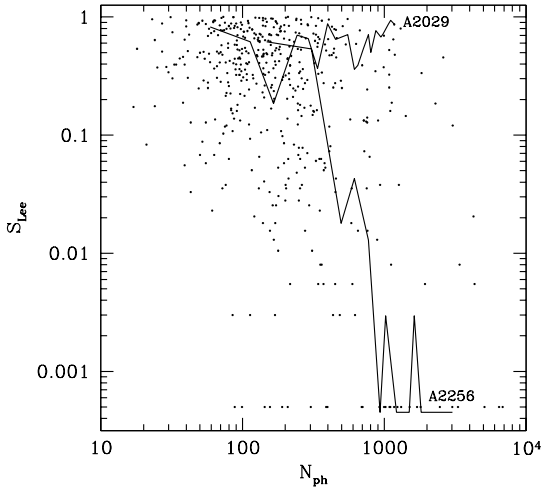

Fig. 4. Distribution of LEE significances as a function of the number of X-ray photons for REFELX+BCS clusters (points), for the substructured cluster A2256 (lower continuous line), and for the cooling flow cluster A2029 (upper continuous line). The lines represent significances obtained with different numbers of X-ray photons selected randomly from the X-ray images. Zero significance values are set to $\sim 5 \times 10^{-4}$.

these numbers with the results obtained with our substructure tests assuming that clusters fulfilling the criterion $\min\{S_{\mathrm{LEE}}, S_\beta\} \leq 0.05$ are substructured. In this case the substructure tests found 46 of the 59 clusters as regular and 11 of the 14 clusters as substructured. This gives a fraction of 22 percent of the clusters with different

classifications. The rate is slightly improved to 21 percent when a significance threshold of 0.01 is used.

Notice that the values of the SORs depend on the details of the sample properties as well as on the actual substructure detection method so that an exact coincidence of SORs obtained with different samples cannot be expected. We conclude that the β and LEE statistic are found to provide useful tools for substructure analysis of RASS-3 X-ray images and can under reasonable conditions approximately verify the Jones & Forman classification scheme.

5. Occurrence rates of clusters with substructure

The observed or apparent frequency of clusters with significant X-ray substructure is the basic quantity of our systematic study which can be determined with high accuracy. The frequency distributions give useful information about the role of substructure and merger events in the nearby Universe, and provide several hints to important selection effects which might bias substructure statistics in general.

For given spatial locations and size of main and subclusters, and for given angular resolution of the X-ray instrument and aperture size, the detectability of substructure depends on the number of X-ray photons, N_{ph}, used to trace the cluster surface brightness distribution, and on the redshift of the cluster. Figure 4 illustrates the N_{ph} effect, plotting the statistical significances for the REFLEX+BCS clusters (dots) as a function of N_{ph}. The superposed continuous lines give sequences of statistical significances obtained for the Abell clusters A2256 and A2029 for different numbers of photons selected randomly from the original RASS-3 photon distribution. A2256 is a well-known example of a cluster merger exhibiting a radio halo and relic. Two subclumps are well-separated in the deeper ROSAT PSPC pointing (Briel et al. 1991, supported by recent CHANDRA results given in Sun et al. 2001), one maximum centered near the central cD galaxy. The cluster is located close to the North Ecliptic Pole so the correspondingly long ROSAT exposure time gives the comparatively large number of 3000 X-ray photons within a circle of 1 Mpc in RASS-3 (hard band, including background photons). A2029 is a cooling flow cluster with a mass deposition rate >550 solar masses per year and a cooling time <3 Gyr (Peres et al. 1998). Buote & Tsai (1996) classified this cluster as regular and smooth and used it as a prototype relaxed single cluster. Within a circle of 1 Mpc about 1100 X-ray photons are found in RASS-3.

For other clusters, and the β and FEL statistic, similar sample paths as shown by the continuous lines in Fig. 4 are found. Therefore, if clusters are located in the upper left part of the $S-N_{\mathrm{ph}}$ diagram with say $S > 0.01$ corresponding to the 99 percent confidence level to reject the null hypothesis, this does not necessarily mean that they do not have any substructure. It only shows that under the actual detection conditions no statistically significant statement about the tested substructure property can be made.
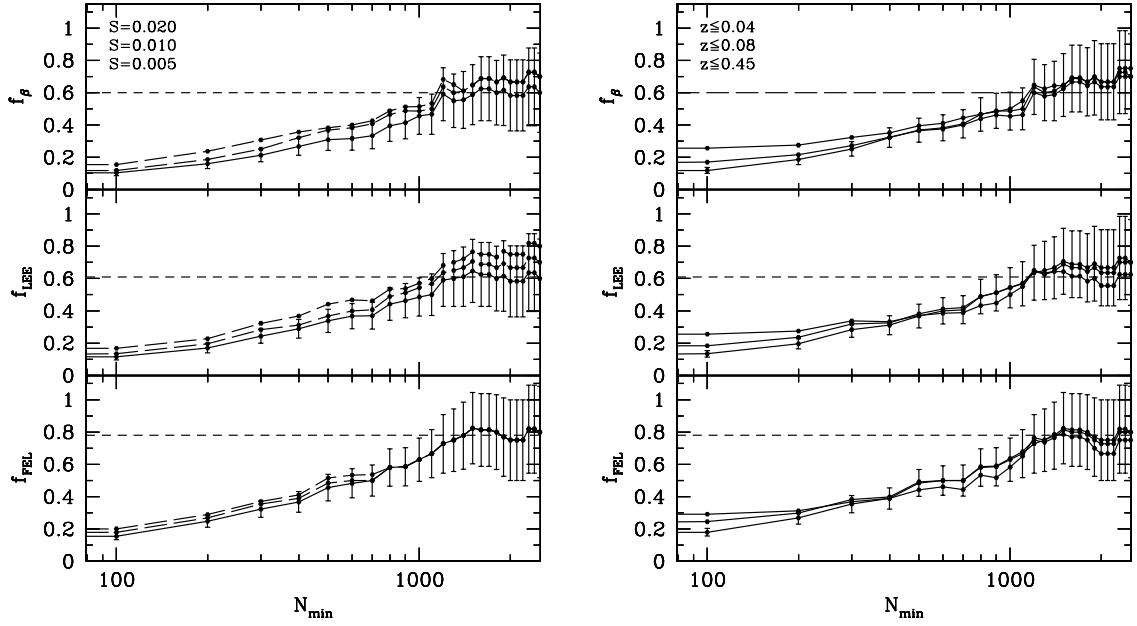
Fig. 5. Left panel: fraction, f, of clusters as a function of the minimum number of X-ray photons, N_{min}, with significances less or equal to the $S = 0.005$ (lower curves with formal Poisson error bars), 0.01 (middle curves) and 0.02 (upper curves) level. In the upper panel the measurements for the $S = 0.01$ and 0.02 levels degenerate above $N_{min} = 1\,400$ whereas for the lower panel all curves degenerate above $N_{min} = 800$. The dashed horizontal lines mark the plateau values obtained for clusters with large numbers of X-ray photons. **Right panel:** same curves as left panel for $S = 0.01$ and the redshift limits $z = 0.04$ (upper curves in each panel, ≤ 88 clusters), $z = 0.08$ (≤ 239 clusters) and 0.45 (≤ 470 REFLEX+BCS clusters).

If more photons are collected the sample paths move to the right of the $S-N_{ph}$ diagram. But whether the path moves up or down would depend on the actual merger situation, the size of the subclusters, and on the cluster's redshift.

The observed occurrence rates, f, of the REFLEX+BCS clusters obtained with the three substructure statistics are plotted in Fig. 5 (left). For the morphological classifications the significance thresholds $S \leq 0.02$, 0.01, and 0.005 are applied. Independent of the corresponding confidence limits the observed fraction of substructured clusters increases with the minimum number of X-ray photons, N_{min}. The comparison of the corresponding diagrams for subsamples of REFLEX+BCS clusters including an upper redshift limit (right panels of Fig. 5) shows that redshift-dependent effects become important for minimum photon numbers $N_{min} \leq 500$. They increase when in addition to an upper redshift limit also a lower limit is introduced. However, the fraction of high-z clusters is small so that their effect on the cumulative distributions is not large. Within the formal 1σ Poisson errors, the observed fractions (complete sample) range between the lower limits of about 10 ± 2 percent and the plateau values of 60 ± 17 percent for the β and LEE statistic, and 78 ± 22 percent for the FEL statistic.

The amplitude and shape of the curves depend on the "true" SOR and the X-ray flux and redshift distributions of the sample clusters which are in the end determined by the structure formation process, on the X-ray telescope and detector angular resolution, on the actual confidence level used for the classification, etc.

5.1. Towards unbiased substructure occurrence rates

Less biased SORs of the REFLEX+BCS clusters can be determined with a kind of template matching procedure where observed and model curves similar to those plotted in Fig. 5 are compared and their differences minimized. The model curves are computed with a set of high signal-to-noise template clusters. This template set has by construction a known substructure occurrence rate, f_{INP}, which can be changed by replacing substructured with regular templates or vice versa. Partially dependent replicants of these templates with different N_{ph} are generated by diluting their X-ray images randomly in the same way as shown by the continuous sample paths in Fig. 4.

For a proper comparison the enlarged set of template images generated by dilution must have the same probability density, $P(N_{ph})$, as the REFLEX+BCS clusters. Precise comparisons would also equalize the redshift distributions of observed and template clusters. This requires, however, a large set of high signal-to-noise X-ray images with at least 1000 X-ray photons at various redshifts. Such a template set is not available yet so that we simply restrict the redshift *range* to be the same for both observed and template clusters.

The matching procedure itself consists for each substructure criterion of the following steps. In the first step the fractions $f(N_{min})$ are computed with the REFLEX+BCS sample (see Fig. 5, left) and for a fixed confidence limit. In the second step an input substructure occurrence rate, f_{INP}, of the template sample is chosen.
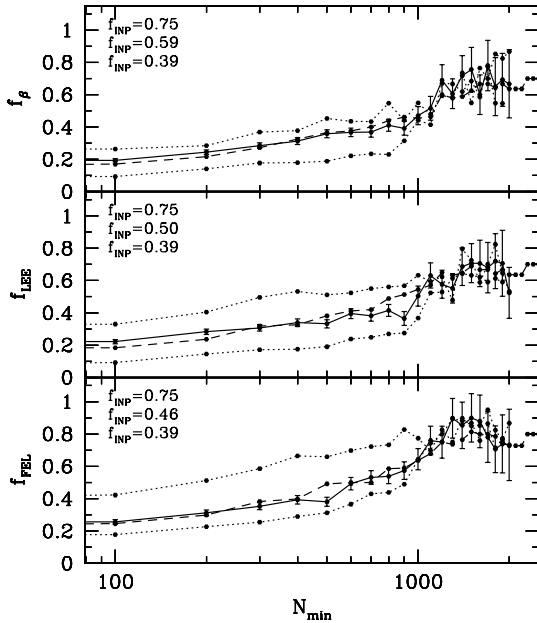
Fig. 6. Significance curves for REFLEX+BCS clusters with redshifts $z \leq 0.08$ (dashed lines) compared to the template samples (continuous lines) covering the same redshift range. The input substructure fractions of the control sample used to fit the observations are shown in the upper left of each panel. The central continuous line represents the best fit of the substructure fraction to the observed curves. All curves are computed for the significance threshold $S = 0.01$.
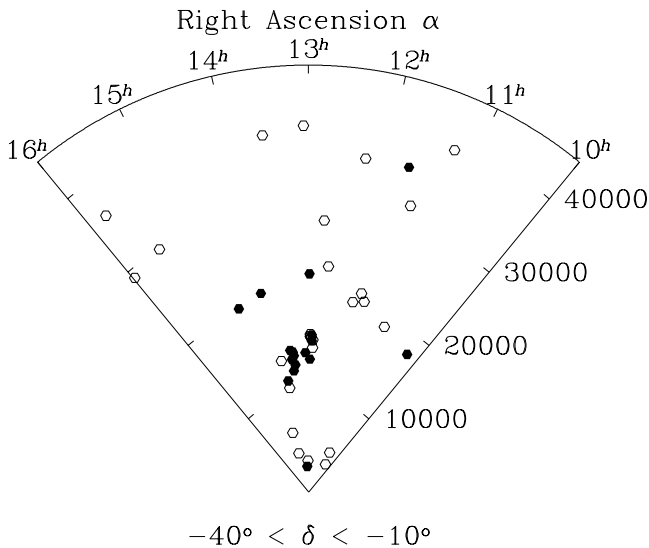

Fig. 7. Spatial distribution of clusters with $\min\{S_\beta, S_{\mathrm{LEE}}\} \leq 0.1$ (filled symbols) and >0.1 (open symbols). The radial coordinate is in $\mathrm{km\,s^{-1}}$. For substructure detection a metric radius of 1 Mpc is used.

The substructure test is computed for the diluted X-ray images. The images are randomly selected in a way that observed and template sets have the same $P(N_{\mathrm{ph}})$ distributions. In the last step the curve, $f(N_{\mathrm{min}})$, is determined and compared with the observed curve. Steps two and

three are iterated by changing f_{INP} of the templates until a useful fit of the observed SOR curve by the template model curve is achieved.

Note that the application of a template sample based on RASS-3 data guarantees that many technical selection effects which might affect the REFLEX+BCS measurements are taken automatically into account. The quality of the results depends on the size and representativity of the template sample.

The results shown in Fig. 6 are computed for a template sample of 37 clusters ($N_{\mathrm{ph}} \geq 1000$) with redshifts $z \leq 0.08$ and different input substructure fractions. Notice that the classification of templates into substructured and regular clusters is done by using literature information of the kind given in Tables 1 and 2, and by visual inspection. As an example, curves are shown for a significance threshold of $S = 0.01$. The results obtained with the 239 REFLEX+BCS clusters are limited to the same maximum redshift as the control sample. Each template cluster is diluted 20 times so that an effective number of 740 partially dependent template clusters is used.

A simultaneous fit of the observed and model curves turns out to be complicated because the shapes of the curves differ systematically when specific N_{min} ranges are considered, indicating the presence of some remaining systematic differences between observed and template samples. One could, for example, expect that the template sample might not be representative of the complete REFLEX+BCS sample. Best (eye-ball) fits (continuous lines) give SORs ranging from 46 percent (FEL) to 59 percent (β).

The reference (dotted) lines give some information about the sensitivity of the results to changes of f_{INP}. They are computed for $f_{\mathrm{INP}} = 0.39$ and 0.75. The flatter FEL curves suggest that elongation is less affected by N_{ph}. This result supports our evaluation of FEL for individual clusters (Sect. 4.2) and is quite important for our planned studies of alignment effects of position angles of major cluster axes.

The final estimate of the "true" SOR is estimated by the formal mean and standard deviation of the three input rates and gives

$$\mathrm{SOR} \;=\; 52 \pm 7 \text{ percent}. \tag{8}$$

Note that this result is independent whether elongation is regarded as substructure because FEL is only used as a link between template and REFLEX+BCS clusters.

The nature of the merger events involved to yield the observed SOR is not clear because the applied substructure tests do not give mass estimates of the individual subclumps. Therefore, numerical simulations are in preparation to decide statistically which merger type (major merger or accretion) contributes at a given redshift and flux to the observed SOR.

Another way to proceed further is the relative comparison of subsamples derived from the REFLEX+BCS sample so that selection effects introduced by the actual

observing conditions partially cancel out. Results obtained with this approach are described in the following sections.

6. Substructure density relation

Clusters in dense (supercluster) environments are expected to have a higher probability to interact with neighbouring clusters or filamentary structures connecting the cluster centers. If this hypothesis is correct, larger fractions of clusters with distorted X-ray surface brightness distributions and thus with subclusters are expected in dense environments.

As an illustrative example, Fig. 7 shows the spatial distribution of the clusters with $\min\{S_\beta, S_{\text{LEE}}\} \leq 0.1$ (filled symbols) and >0.1 (open symbols) in a region located at the Shapley concentration. It is seen that clusters with a lower significance to have a regular RASS-3 image (filled symbols) appear to be preferentially more concentrated towards the core of the Shapley supercluster. If the significance threshold of 0.1 is lowered to 0.01 basically all clusters expected to show substructure are located in the Shapley concentration (only one cluster lies outside the supercluster). The effect thus seems to be not very sensitive to the actual value of the significance threshold applied. Similar but less extreme trends are found for other supercluster regions.

To quantify this effect and to test its statistical significance, mean significances of β and LEE (for completeness we also use FEL) are computed for different local cluster number densities. For volume-limited samples, the computation of local cluster number densities would be straightforward. The REFLEX and BCS cluster samples used for the present investigation are, however, X-ray flux-limited and, although the samples are the largest yet available, volume-limited subsamples derived from them have sample sizes smaller than about 100 (see, e.g., Table 1 in Schuecker et al. 2001). If we would further subdivide these subsamples with respect to different morphological classes the results would immediately suffer from small-number statistics. Therefore, we decided to work with flux-limited samples although the definition of redshift-independent measures of local cluster number density becomes less well-defined.

As a measure of the local cluster number density around each cluster we use $\bar{d}^{-3}$, where $\bar{d}$ is the mean of its 5 nearest neighbour distances. In order to correct for the redshift dependence of the cluster number density in flux-limited cluster samples, we normalize this number density by the average density obtained with the same density estimator using all clusters in a redshift shell $(z - \Delta z, z + \Delta z)$ centered on the cluster's z value (see comments given in Sect. 8). The normalization has the additional effect of compensating also for edge effects which are known to distort next neighbour statistics (e.g., Cressie 1993).

The flux limit of REFLEX+BCS is quite bright and the segregation effect quite large (see below) so that it is not necessary to correct for local variations of the REFLEX and BCS survey sensitivity (e.g., RASS

exposure convolved with galactic extinction). Note that cluster X-ray fluxes are, however, corrected for galactic extinction. Furthermore, no corrections for chance contamination of cluster images by non-cluster sources are applied because results obtained with different cluster subsamples drawn from the same parent distribution are compared.

For the analysis of the REFLEX+BCS sample the average cluster number densities, $\bar{n}$, are computed within redshift shells with $\Delta z = 0.01$ centered at the cluster redshifts. The local density contrasts are compared with the centers of optical superclusters given in Zucca et al. (1993). Among others, the Perseus-Pisces, Corona-Borealis, Hercules, Shapley, and Horologium superclusters are clearly detected as regions with $n/\bar{n} > 1$ for the majority of the supercluster members.

Figure 8 (left) shows the average substructure significances as a function of the local cluster number density contrasts excluding the very extreme contrasts where sample sizes are small and the results quite noisy. The bars represent the formal 1σ errors (excluding cosmic variance). It is seen that the average significances of β and LEE decrease with density contrast. The effect is supported by subsamples of nearby clusters with comparatively large numbers of X-ray photons. In addition, we compare the sensitivity of the results to boundary effects possibly introduced by the galactic plane. The same trends are found (although with larger scatter) if only those clusters where the maximum distance of the 5th neighbour cluster is far away from any survey boundary were analyzed.

The same effect appears also on a larger metric scale when the aperture radius for substructure detection is increased from 1 Mpc to 3 Mpc (see Fig. 8, right). Here we could follow the trend to even higher density contrasts, although error bars get quite large. For the latter case we can, however, not rule out that neighbouring clusters not necessarily in the process of merging with the programme cluster might artificially increase the SORs (notice that the average significances are in general lower for the 3 Mpc apertures compared to the 1 Mpc results). In addition, many clusters have significance radii smaller than 3 Mpc especially at lower redshift so that the effect of background sources or local variations of the X-ray background appears to be less clear.

To summarize, if the β and LEE statistics are regarded as reliable indicators for substructure (see Sect. 4) then the results shown in Figs. 7 to 8 clearly indicate that the fraction of substructured clusters increases with local cluster number density.

Contrary to the results obtained with β and LEE, the average elongation significances are found to be almost insensitive to local cluster number density contrasts. A decrease of $\langle S_{\text{FEL}} \rangle$ might be indicated on the 3 Mpc scale, but the effect seems to be not very strong. A constant value is just consistent with the 1σ confidence limit. The different behaviour of FEL is not yet fully understood. However, as noted in Sect. 4, the presence of elongation is not necessarily restricted to merger events so that low
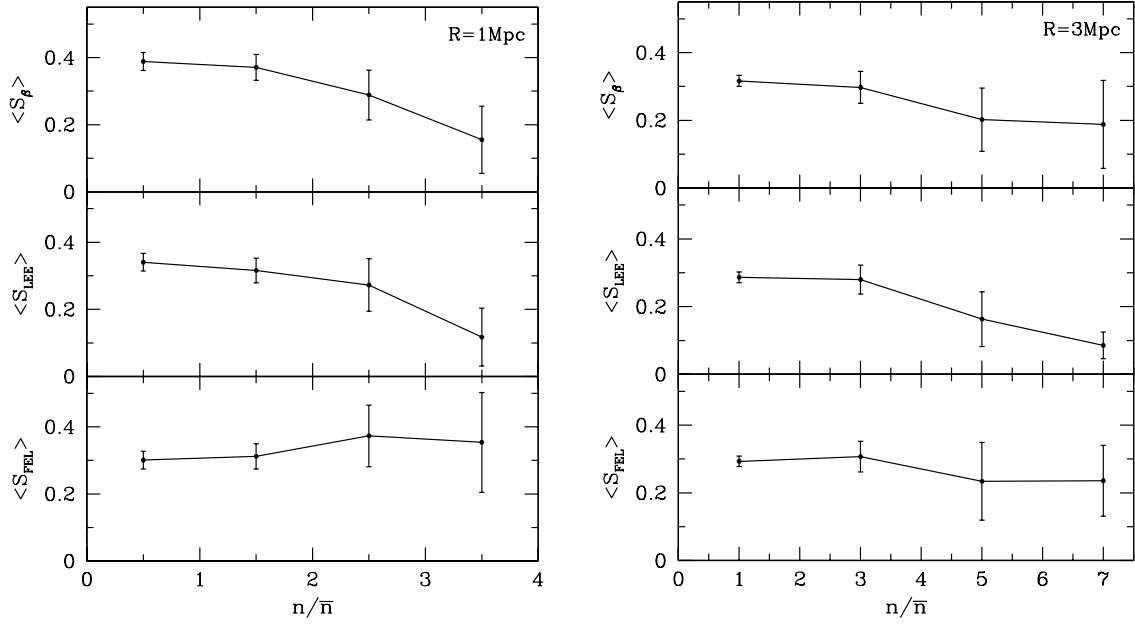
Fig. 8. Left: average significances and their standard deviation for the three statistical tests as a function of the local cluster number density, normalized to the average density for an aperture radius of 1 Mpc. **Right:** same as left for an aperture radius of 3 Mpc.
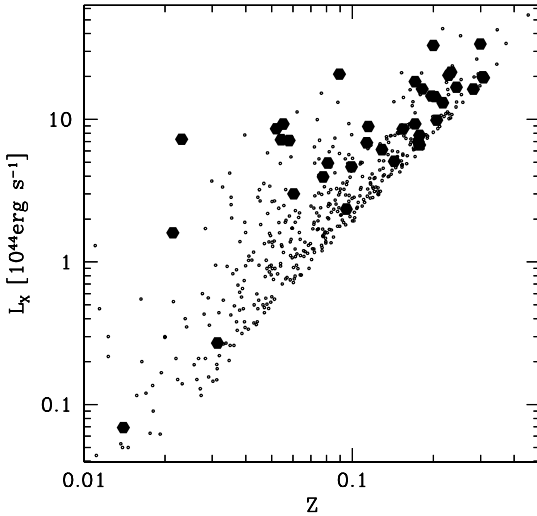

Fig. 9. X-ray luminosity versus redshift for REFLEX+BCS clusters (small points) and for halo and relic clusters (filled circles).

$<S_{\mathrm{FEL}}>$ values are expected in both high and low-density regions, which could reduce a density-dependent effect.

7. Substructures in halo, relic, and cooling flow clusters

Radio halo and relic clusters are found among the most X-ray luminous galaxy clusters. This is shown in Fig. 9 where the X-ray luminosity in the energy band 0.1–2.4 keV is plotted as a function of redshift for the REFLEX+BCS

reference sample (dots), and the halo/relic clusters (filled circles). A threshold luminosity, $L_{\mathrm{X}} = 4.0 \times 10^{44}\,\mathrm{erg\,s^{-1}}$, might be introduced above which most of the halo/relic clusters are located. In the following we assume that the given halo/relic sample is representative and compare the observed fractions of halo/relic clusters with substructured RASS-3 X-ray images with the corresponding results obtained for cooling flow and REFLEX+BCS clusters.

For a proper comparison of the frequencies of clusters with substructure obtained with different samples one has to equalize the efficiencies of substructure detection which might be different for the samples. Section 5 shows that the number of photons per target, N_{ph}, is the most crucial factor determining the efficiency of substructure detection (the redshift bias will be discussed below). The first step thus is to equalize the frequency distributions of N_{ph} for the different samples.

Both the halo/relic and the cooling flow samples have on average higher X-ray fluxes yielding more X-ray photons per cluster target compared to a typical REFLEX+BCS cluster. Therefore, the REFLEX+BCS sample is in general less sensitive to substructure detection compared to the other samples. The naive comparison of the substructure tests would thus lead to a systematic underestimation of the frequency of substructure for REFLEX+BCS clusters.

In order to correct for the systematic effect one has to dilute a larger reference sample so that its normalized cumulative probability distribution function, $P(<N_{\mathrm{ph}})$, resembles the distribution function of a smaller test sample. The dilution is performed as in standard Monte Carlo experiments by randomly selecting from a uniform
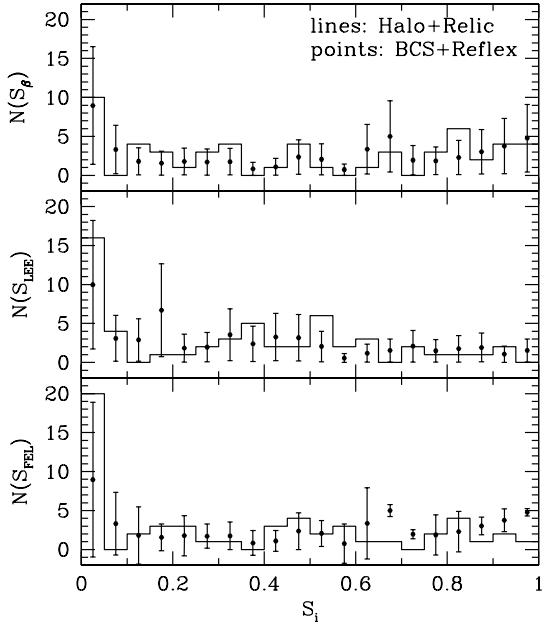
Fig. 10. Frequency distributions of substructure significances of halo/relic clusters (lines) and Reflex+BCS clusters (points). The computation of the latter frequencies and their 1σ standard deviations is described in the text.
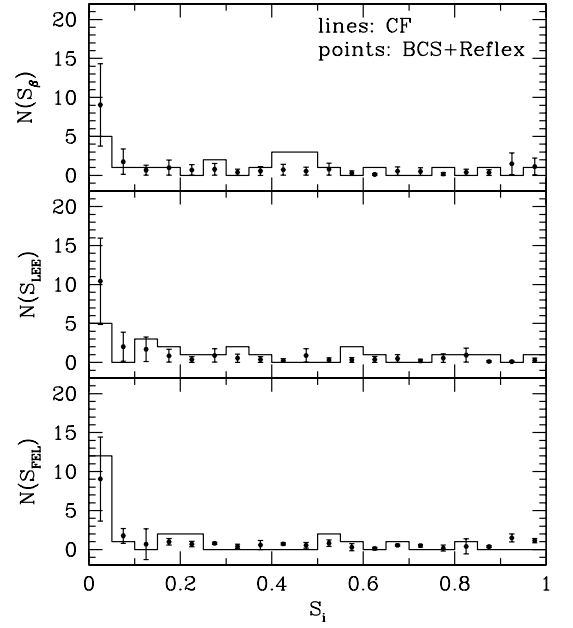

Fig. 11. Frequency distributions of substructure significances of cooling flow clusters (lines) and Reflex+BCS clusters (points). The computation of the latter frequencies and their 1σ standard deviations is described in the text.

distribution a number between 0 and 1, computing the corresponding $N'_{\rm ph}$ value as given by the distribution function of the test sample, and selecting the reference cluster with a $N_{\rm ph}$ value next to $N'_{\rm ph}$. These steps are repeated until the replicant of the reference sample has the same sample size as the test sample. In order to get more representative results many replicants of the reference sample are created, giving better estimates of the mean values and their standard deviations.

The resulting significance frequency distributions and their 1σ errors (points with error bars, see below) are given in Figs. 10 to 12. Notice that the latter figure compares halo/relic clusters with cooling flow clusters. In this case the halo/relic sample is used as reference. The standard deviations (error bars) are computed in the following way. As mentioned above the reference sample is diluted so that its sample size and photon number distribution resembles either the halo/relic, or cooling flow sample. For each cluster type this is done 20 000 times. The standard deviation is estimated from the scatter of the numbers of clusters selected in each significance bin (a kind of Bootstrap error).

It should be noted that the following analysis is restricted to a discussion of the frequencies of the significances obtained for circular symmetry (β), unimodality (LEE), and mirror symmetry (FEL) for different cluster types. Therefore, the introduction of a specific confidence level is not necessary. The results presented here do also not depend on the specific binning used to count the frequencies of the significance values. The following statements on the significances are based on the frequencies and their errors obtained in the first S bin because here
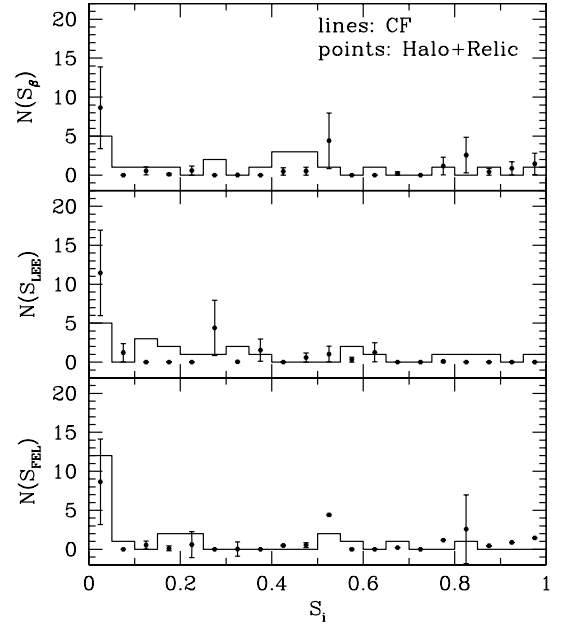

Fig. 12. Frequency distributions of substructure significances of cooling flow clusters (lines) and halo+relic clusters (points). The computation of the latter frequencies and their 1σ standard deviations is described in the text.

the differences in the substructure behaviour are most interesting.

The comparison indicates that halo/relic, cooling flow, and REFLEX+BCS clusters do not strongly differ in their substructure behaviour. The differences found in the RASS-3 images between these types are all on the 1–$2\,\sigma$

level. However, the general picture that cooling flow clusters appear to be more regular and halo/relic clusters more often substructured is supported. In the following more specific results are described.

Comparison of halo/relic with REFLEX+BCS clusters (see Fig. 10): halo and relic clusters are found to have high frequencies for all three substructure tests below $S = 0.05$ compared to REFLEX+BCS, suggesting that halo and relic clusters appear to be on average more substructured compared to REFLEX+BCS clusters. Whereas the excess is only marginal for β, about 1σ excesses are found for both LEE and FEL. Halo/relic clusters thus appear more often bi-modal and elongated compared to other cluster types.

Comparison of cooling flow with REFLEX+BCS clusters (see Fig. 11): cooling flow clusters are found to have lower frequencies in the $S \leq 0.05$ bin for β and LEE whereas a small excess is found for FEL compared to the REFLEX+BCS reference sample. The deviations are on the 1σ level, but in the opposite direction as found for the halo/relic clusters in Fig. 10. The measurements thus suggest that clusters with large cooling flow signatures appear to be more often circular symmetric and unimodal. Significant elongations of their X-ray images are found slightly more often compared to REFLEX+BCS clusters.

Comparison of cooling flow with halo/relic clusters (see Fig. 12): cooling flow clusters are found to have more often circular symmetric and unimodal RASS-3 images compared to halo/relic clusters. Moreover, cooling flow clusters appear to be marginally more often elongated.

8. Discussion

A systematic study of the morphologies of RASS-3 images of BCS and REFLEX clusters is given. The two surveys provide the largest presently available X-ray cluster samples and are expected to yield statistically representative results. Our analysis shows that many observational effects lead to systematic errors in the statistic of merger events. After approximate corrections are applied an estimate of the SOR of 52 ± 7 percent is found. This number might also be contaminated by chance superposition of point-like (background) sources. However, the effects are expected to be small because a comparatively small aperture radius of 1 Mpc for substructure measurements is used.

How does this SOR estimate compares with the results obtained with similar projects in X-rays? As mentioned above, with 208 *Einstein* IPC images Jones & Forman (1999) find by visual inspection a SOR of 41 percent. With 65 *Einstein* IPC images Mohr et al. (1995) used the emission-weighted centroid variation for substructure detection. Kolmogorov-Smirnov tests suggests that the sample is representative. They found a SOR of 61 percent for the same confidence level (99 percent) as used for the REFLEX+BCS sample.

It is thus seen that the three largest presently available systematic X-ray cluster works give SORs of about 50 percent. However, the conservative (formal) 3σ standard deviation of 30 percent between the three estimates already indicates that there is still considerable scatter between different samples and methods. The conservative interval of substructure occurrence rates

$$20 \leq f \leq 80 \text{ percent } (99\%, \text{confidence range}), \qquad (9)$$

for nearby clusters with $z < 0.15$ might give a realistic impression of the current situation of statistical work on X-ray SORs.

The next step towards a physical understanding of the observed SOR should be the determination of the mass scales of the subclumps and the dynamical time scales involved. Note that the individual contributions of major mergers and accretion to (9) are not given by the measurements. Obtaining quantitative estimates appears to be quite difficult, even if the analysis would have been done with better data and refined substructure tests.

However, large sample sizes offer the possibility to calibrate the substructure events at least in a statistical manner by the application of the same substructure tests to both observed and simulated X-ray cluster images distributed in flux and redshift in the same way. The simulation will also include a realistic X-ray background so that an artifical increase of the observed SOR through background point sources (see above) is taken into account. Simulations of this kind would establish the link between substructure as defined by the various measures and the dynamical state of a cluster (Schuecker et al., in preparation). Some interesting statistical results deduced from the combination of observational work and numerical experiments can be found in, e.g., Mohr et al. (1995).

Depending on the accuracy of this comparison one should also try to investigate redshift-dependent effects where no information is available yet. High-resolution N-body simulations of, e.g., Gottlöber et al. (2001) suggest an increase of major merger rates by a factor of about 2 between redshift $z = 0$ and 0.25.

Almost independent from the observational effects mentioned above the relative comparison of cluster subsamples show that the fraction of clusters with X-ray substructure turns out to be a function of local cluster number density in the sense that the fraction of clusters with low statistical significances for circular symmetric and unimodal X-ray surface brightness distributions increases with local cluster number density. Such a substructure-density relation is expected when the merging of subclusters causes the observed substructures. Although the analyses are based on the largest presently available X-ray cluster catalogue, we were forced to use flux-limited subsamples in order to get statistically significant results. When larger X-ray cluster samples are available, future studies will allow the extraction of statistically significant *volume-limited* subsamples. This will give a better defined cluster number density with the additional

benefit of rough mass estimates as obtained from the mass X-ray luminosity relation of Reiprich & Böhringer (2001).

The substructure-density relation of clusters appears to be analogous to the morphology-density relation of galaxies. A related effect, namely that dynamically young optical APM clusters are more clustered than the overall cluster population was recently found by Plionis (2001) thus supporting the present findings.

The relative abundances of radio halo, relic, and cooling flow clusters with substructures could be studied in more detail. Whereas halo and relic clusters tend to show more often substructure in RASS-3, cooling flow clusters show the opposite effect. Notice that the comparisons of cooling flow clusters either with REFLEX+BCS (Fig. 11) or with halo/relic clusters (Fig. 12) give quite similar results supporting their robustness because almost independent reference samples are used. We thus regard the finding that cooling flow cluster show in general more often regular and unimodal X-ray surface brightness distributions than other cluster types as quite stable. Notice that a fraction of $5/22 = 0.23$ cooling flow clusters show either $S_{\mathrm{LEE}} = 0$ or/and $S_\beta = 0$ indicating that substructured cooling flow clusters are to be expected. In addition, a fraction of $7/22 = 0.31$ have $S_{\mathrm{FEL}} \leq 0.01$ indicating that one third of the cooling flow clusters show significant elongation within the inner $1\,\mathrm{Mpc}$ radius, possibly impressed by the cD galaxy.

On the other hand, although halo and relic clusters show more often bi-modal and elongated RASS-3 surface brightness distributions, they appear to share more similarities with other cluster types than cooling flow clusters.

Nevertheless, our analyses give additional support to the idea that cluster mergers might trigger the formation of radio halos and relics whereas pre-existing cooling flows might be disrupted by recent merger events.

References

Böhringer, H., Feretti, L., & Schuecker, P. 1999, proceedings Diffuse Thermal and Relativistic Plasma in Galaxy Clusters, MPE Report 271

Böhringer, H., Voges, W., Huchra, J. P., et al. 2000, ApJS, 129, 435

Böhringer, H., Schuecker, P., Guzzo, L., et al. 2001, A&A, 369, 826

Briel, U. G., Henry, J. P., Schwarz, R. A., et al. 1991, A&A, 246L, 10

Buote, D. A. 2001, in Merging Processes in Clusters of Galaxies, ed. L. Feretti, I. M. Gioia, & G. Giovannini (Dordrecht: Kluwer), in press

Buote, D. A., & Tsai, J. C. 1996, ApJ, 458, 27

Burns, J. O., Roettiger, K., Pinkney, J., et al. 1995, ApJ, 446, 583

Cohen, A. S., Clarke, T. E., Kassim, N., Enßlin, T. A., & Neumann, D. 2001 [`astro-ph/01`]

Cressie, N. A. C. 1993, Statistics for Spatial Data (John Wiley & Sons, New York), 602

Crone, M. M., Evrard, A. E., & Richstone, D. O. 1996, ApJ, 467, 489

de Grandi, S., Molendi, S., Böhringer, H., Chincarini, G., & Voges, W. 1997, ApJ, 486, 738

Ebeling, H., Edge, A. C., Böhringer, H., et al. 1998, MNRAS, 301, 881

Ebeling, H., & Wiedenmann, G. 1993, Phys. Rev. E, 47, 704

Edge, A. C., Steward, G. C., Fabian, A. C., & Arnaud, K. A. 1990, MNRAS, 245, 559

Evrard, A. E., Mohr, J. J., Fabricant, D. G., & Geller, M. J. 1993, ApJ, 419, L9

Fabian, A. C., Nulsen, P. J., & Canizares, C. R. 1984, Nature, 310, 733

Feretti, L. 1999, in Diffuse Thermal and Relativistic Plasma in Galaxy Clusters, ed. H. Böhringer, L. Feretti, & P. Schuecker, MPE Report 271, 3

Feretti, L., Giovannini, G., in Extragalactic Radio Sources, ed. R. Ekers, C. Fanti, & L. Padrielli (Dordrecht: Kluwer), 333

Fitchett, M. 1988, MNRAS, 230, 161

Fitchett, M. J., & Webster, R. L. 1987, ApJ, 317, 653

Giovannini, G. 1999, in Diffuse Thermal and Relativistic Plasma in Galaxy Clusters, ed. H. Böhringer, L. Feretti, & P. Schuecker, MPE Report 271, 13

Giovannini, G., & Feretti, L., 2000, NewA, 5, 335

Giovannini, G., Tordi, M., & Feretti, L. 1999, NewA, 4, 141

Gottlöber, S., Klypin, A., & Kravtsov, A. V. 2001, ApJ, 546, 223

Hanisch, R. J. 1982, A&A, 116, 137

Harris, D. E., Lari, C., Vallee, J. P., & Wilson, A. S. 1980, A&AS, 42, 319

Jones, C., & Forman, W. 1999, ApJ, 511, 65

Kolokotronis, V., Basilakos, S., Plionis, M., & Georgantopoulos, I. 2000 [`astro-ph/0002432`]

Lacey, C., & Cole, S. 1993, MNRAS, 262, 627

Makishima, K., et al. 2001, PASJ, accepted, see also [`astro-ph/0104079`]

Markevitch, M., et al. 2000, ApJ, 541, 542

Mohr, J. J., Evrard, A. E., Fabricant, D. G., & Geller, M. J. 1995, ApJ, 447, 8

Owen, F., Morrison, G., & Voges, W. 1999, in Diffuse Thermal and Relativistic Plasma in Galaxy Clusters, ed. H. Böhringer, L. Feretti, & P. Schuecker, MPE Report 271, 9

Peebles, P. J. E. 1980, The Large-Scale Structure of the Universe (Princeton University Press: Princeton, New Jersey)

Peres, C. B., Fabian, A. C., Edge, A. C., et al. 1998, MNRAS, 298, 416

Peterson, J. R., et al. 2001, A&A, 365, L104

Peterson, J. R. 2001, A&A, 365, L87

Pinkney, J., Roettiger, K., Burns, J. O., & Bird, C. M. 1996, ApJS, 104, 1

Plionis, M. 2001 [`astro-ph/0105522`]

Reiprich, T. H., & Böhringer, H. 2001, ApJ, submitted

Rhee, G. F. R. N., van Haarlem, M. P., & Katgert, P. 1991, A&AS, 91, 513

Richstone, D., Loeb, A., & Turner, E. 1992, ApJ, 393, 477

Ricker, P. M., & Sarazin, C. L. 2001 [`astro-ph/0107210`]

Roettiger, K., Loken, C., & Burns, J. O. 1997, ApJS, 109, 307

Roettiger, K., Stone, J. M., & Burns, J. O. 1999, ApJ, 518, 594

Sarazin, C. L. 2001, in Merging Processes in Clusters of Galaxies, ed. L. Feretti, M. Gioia, & G. Giovannini (Dordrecht: Kluwer), in press

Schindler, S., & Müller, E. 1993, A&A, 272, 137

Schuecker, P., Böhringer, H., Guzzo, L., et al. 2001, A&A, 368, 86

Sun, M., Murray, S. S., Markevitch, M., & Vikhlinin, A. 2001 [astro-ph/0103103]

Takizawa, M. 2000, ApJ, 532, 183

Thomas, P. A., et al. (the Virgo Consortium) 1998, MNRAS, 296, 1061

Trümper, J. 1993, Science, 260, 1769

Voges, W., Aschenbach, B., Boller, Th., et al. 1999, A&A, 349, 389

West, M. J., Oemler, A. Jr., & Dekel, A. 1988, ApJ, 327, 1

White, S. D. M. 1996, in Cosmology and Large-Scale Structure, ed. R. Schaeffer, J. Silk, M. Spiro, & J. Zinn-Justin (Elsevier, Dordrecht), 349

Willson, M. 1970, MNRAS, 151, 1

Vikhlinin, A., Markevitch, M., & Murray, S. M. 2001, ApJ, 549, L47

Zucca, E., Zamorani, G., Scaramella, R., & Vettolani, G. 1993, A&A, 407, 470